LINK TO ONLINE ABSTRACT IN THE OSA JOURNAL:

https://www.osapublishing.org/boe/fulltext.cfm?uri=boe-12-6-3392&id=451065

Check for updates

The LUCA device: a multi-modal platform combining diffuse optics and ultrasound imaging for thyroid cancer screening

LORENZO CORTESE,[1,14,*] GIUSEPPE LO PRESTI,[1,14] MARTA ZANOLETTI,[2] GLORIA ARANDA,[3] MAURO BUTTAFAVA,[4] DAVIDE CONTINI,[2] ALBERTO DALLA MORA,[2] HAMID DEHGHANI,[5] LAURA DI SIENO,[2] SIXTE DE FRAGUIER,[6] FELICIA A. HANZU,[3,7,8] MIREIA MORA PORTA,[3,7,8] AN NGUYEN-DINH,[9] MARCO RENNA,[4,10] BOGDAN ROSINSKI,[9] MATTIA SQUARCIA,[3,11] ALBERTO TOSI,[4] UDO M. WEIGEL,[12] STANISLAW WOJTKIEWICZ,[5] AND TURGUT DURDURAN[1,13]

[1]*ICFO-Institut de Ciències Fotòniques, The Barcelona Institute of Science and Technology, 08860 Castelldefels (Barcelona), Spain*
[2]*Politecnico di Milano, Dipartimento di Fisica, 20133 Milano, Italy*
[3]*IDIBAPS, Fundació Clínic per la Recerca Biomèdica, Barcelona, Spain*
[4]*Politecnico di Milano, Dipartimento di Elettronica Informazione e Bioingegneria, 20133 Milano, Italy*
[5]*University of Birmingham, School of Computer Science, Edgbaston, Birmingham, B15 2TT, UK*
[6]*IMV Imaging, 16000 Angoulême, France*
[7]*Endocrinology and Nutrition Department, Hospital Clínic of Barcelona, Barcelona, Spain*
[8]*Centro de Investigación Biomèdica en Red Diabetes y Enfermedades Metabólicas Asociadas (CIBERDEM), Spain*
[9]*VERMON S.A., 37000 Tours, France*
[10]*Athinoula A. Martinos Center for Biomedical Imaging, MGH, Harvard Medical School, Charlestown, MA 02129, USA*
[11]*Neuroradiology Department, Hospital Clínic of Barcelona, Barcelona, Spain*
[12]*HemoPhotonics S.L., 08860 Castelldefels (Barcelona), Spain*
[13]*Institució Catalana de Recerca i Estudis Avançats (ICREA), 08015 Barcelona, Spain*
[14]*These authors equally contributed to this work. Authors are listed in alphabetical order except for the first three and the last*
[*]*lorenzo.cortese@icfo.eu*

Abstract: We present the LUCA device, a multi-modal platform combining eight-wavelength near infrared time resolved spectroscopy, sixteen-channel diffuse correlation spectroscopy and a clinical ultrasound in a single device. By simultaneously measuring the tissue hemodynamics and performing ultrasound imaging, this platform aims to tackle the low specificity and sensitivity of the current thyroid cancer diagnosis techniques, improving the screening of thyroid nodules. Here, we show a detailed description of the device, components and modules. Furthermore, we show the device tests performed through well established protocols for phantom validation, and the performance assessment for *in vivo*. The characterization tests demonstrate that LUCA device is capable of performing high quality measurements, with a precision in determining *in vivo* tissue optical and dynamic properties of better than 3%, and a reproducibility of better than 10% after ultrasound-guided probe repositioning, even with low photon count-rates, making it suitable for a wide variety of clinical applications.

1. Introduction

Over the last two decades, multi-modal instrumentation combining near-infrared diffuse optical spectroscopy and ultrasound (US) began to emerge in clinical research and applications [1–4]. The bulk of this work focused on oncological applications where the optical methods are hypothesized to provide complementary physiological information to ultrasound and other modalities. US is utilized as a convenient and clinically accepted modality to guide the optical measurements by identifying the right region of interest, and by providing information about the geometry of the underlying tissue, which, in turn, is used to improve the accuracy and the precision of the optical data analysis [5–11].

Diffuse optical technologies utilize near-infrared light ($\sim 650 - 950$ *nm*) [12,13] and have gathered interest for testing for a broad range of potential clinical applications [14–21]. They are relatively unique since they can probe deep (>1 cm) tissues in a non-invasive, safe manner to recover important quantitative information about tissue hemodynamics, components and structural features. These parameters are speculated to be important biomarkers of both healthy functioning tissue and its pathology [12].

Near-infrared time resolved spectroscopy (TRS) [22–24] utilizes short laser pulses (~ 100 *ps*) at multiple wavelengths and measures their delay and broadening after having traveled through the tissue. It is capable of determining the absolute values of tissue optical properties such as the wavelength dependent absorption and reduced scattering coefficients, which are then used to retrieve physiological quantitative information. Of particular interest are the concentration of oxy- and deoxy-hemoglobin species, which are used to derive the microvascular blood oxygenation and blood volume. Other important components often measured by TRS are collagen, water and lipid concentrations [25,26]. In addition, the measurement of the scattering coefficient can provide important information about tissue cellular structure [27,28].

Diffuse correlation spectroscopy (DCS) [12,29,30], on the other hand, uses a continuous wave coherent laser source and exploits the decay of the speckle intensity auto-correlation function due to light scattering by moving particles (i.e. red blood cells) to measure the bulk microvascular blood flow of the probed tissue volume.

Separately, DCS and TRS only offer limited information about tissue physiology, but, the simultaneous combination of the information provided by TRS and DCS allows to retrieve complementary information about hemodynamics, oxygen metabolism, composition and structure of the measured tissue, enhancing the sensitivity to those biomarkers that important to discriminate between healthy and pathological conditions. This has been successfully exploited in several clinical research studies, from adult and infant brain monitoring to cancer diagnosis and therapy monitoring [31–38].

In this context, a consortium titled "Laser and Ultrasound Co-Analyzer for thyroid nodules" (LUCA) has been formed, funded by the European Commission (see Appendix) [39]. The overall goal of the LUCA project is to develop a multi-modal point-of-care device, combining time resolved spectroscopy, diffuse correlation spectroscopy and medical ultrasound imaging in a single platform with the aim of improving the screening of thyroid nodules for cancer.

Thyroid nodules are a common pathology having a prevalence of palpable nodules of around 5% in women and 1% in men, and, when neck ultrasound is used for screening, the prevalence increases to 19-76% [40,41]. The current established diagnosis protocols for assessing the malignancy of a nodule envisage the thyroid examination with ultrasound and ultrasound Doppler, followed by a fine needle aspiration biopsy (FNAB). Unfortunately, these diagnosis procedures have limited effectiveness, lacking in specificity and sensitivity (ranging from 10-87% in sensitivity to 58-96% in specificity depending on the type of the malignant nodules), and lead to a large number of non-diagnostic and/or false positives, resulting in unnecessary surgeries [42–46].

LUCA platform will try to address the poor sensitivity and specificity of current thyroid cancer screening protocols by providing at the same time information about anatomy (through the medical US imaging), tissue hemodynamics (microvascular blood flow, blood oxygenation), and chemical constitution (collagen, water and lipid concentrations, and scattering spectrum) of the tissue examined [10,25,47].

In the following sections, we present the detailed description of the LUCA device, considering all the separate modules and their integration in a single device, together with the tests performed in tissue mimicking phantoms and *in vivo*.

2. LUCA device and methods

LUCA aim is to be integrated inside the current thyroid nodule screening work-flow, by providing additional physiological information simultaneously to the clinical ultrasound examination performed by the medical doctor. For this purpose, all the different technologies of LUCA have been embedded in a single device. A unique multi-modal probe, including both the US transducer and the optical fibers, has been developed to allow the simultaneous acquisition of optical and US signals. For the same purpose, the LUCA prototype has been built in such a way that the measurement protocol can be managed by the medical doctor through the US touch-screen interface, capable of visualizing and storing the results of optical measurements together with the real time ultrasound images. An additional software and a separate monitor have been added to control and set advanced parameters related to the optical subsystems as needed, which is particularly important during the first clinical measurement campaigns to optimize the optical parameters and measurement protocols.

A photo of the LUCA device is shown in Fig. 1(a), together with the LUCA probe (b), and a diagram of the different modules of the device (c). The modules are: a time resolved spectroscopy module (TRSM), a diffuse correlation spectroscopy module (DCSM), an ultrasound module (USM), a multi-modal optical-ultrasound probe, a main control module (MM) responsible of the control and communication with all the other modules, and a post processing evaluation module based on NIRFAST software (NIRFAST evaluation module, NEM) [48]. In addition, the LUCA device includes an uninterruptible power supply, an emergency shut-down button, and a medical grade isolation transformer.

2.1. Time resolved spectroscopy module (TRSM)

The TRSM - described as a stand-alone system in a separate publication [49] - has been developed by LUCA partner Politecnico di Milano. It is hosted in a 19" case ($48 \times 38 \times 20 \ cm^3$) and has eight gain-switched laser diode sources, with wavelengths in the range $635 - 1050 \ nm$, that are driven at a repetition rate of 40 *MHz* by a custom-made electronic control board with low-jitter logic. Such laser sources feature a temporal jitter of about 140 *ps* (full width half maximum, FWHM), with output powers greater than 1 *mW*.

Laser outputs are coupled with standard graded index (GRIN) $100/140 \ \mu m$ core/cladding diameter fibers, which, in turn, are the input of a 9×1 optical switch (Piezosystem Jena, Germany), which selects the wavelength that is injected sequentially into the sample through standard GRIN fibers.

Diffuse photons are recollected at two source-detector distances by using two compact silicon photomultipliers (SiPM) detectors, which show state-of-the-art performances compared to bulky, expensive and fragile traditional systems based on photomultiplier tubes. Notch filters (Semrock, U.S.A.) have been added in front of the detectors to filter out the DCS source light at 785 *nm*, allowing simultaneous DCS and TRS acquisition.

Two time-to-digital converters (TDC), developed in application specific integrated circuits (ASIC) and integrated onto a field programmable gate array (FPGA) board, reconstruct the
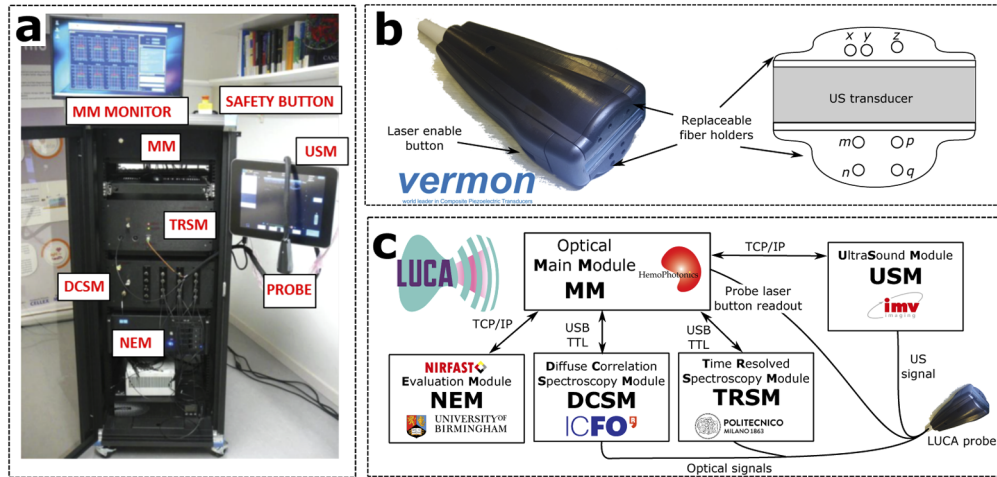
Fig. 1. (a) Photo of the LUCA device, with all the modules. (b) Photo of the LUCA multi-modal optical-ultrasound probe, with a sketch of the probe nose showing the current geometrical disposition of the fiber tips: $x − y$ DCS source fibers; z TRS source fiber, $m − n$ DCS detection fibers, $p − q$ TRS detection fibers. (c) Block diagram of the LUCA device modules and communication.

distribution of time-of-flight of photons (DTOF) up to count-rates of 3 *Mcounts/s* with a timing resolution of about 10 *ps*.

2.2. Diffuse correlation spectroscopy module (DCSM)

The DCSM is a custom DCS device built at ICFO. It is mounted in an independent 19" case, with a independent medical grade modular power supply.

The DCSM source is custom made by LUCA partner HemoPhotonics S. L., and consists of a fiber coupled single longitudinal mode continuous wave laser emitting at 785 *nm*, with a typical operation power of 70 *mW*. An optical clean up filter at 785 *nm* (Semrock, U.S.A.) is inserted in the laser module to remove the tails of the laser spectral emission. The emitted light is split by a fiber beam splitter into two equal intensity branches, allowing the DCSM having two laser outputs coherent with each other, that is, with the relative phase constant over a time longer than the acquisition time of every correlation curve. The intensity of each output is tunable by two fiber optical attenuators. For the *in vivo* measurements, each fiber's power output has been limited to 27 *mW* to respect the safety limits established by American National Standards Institute (ANSI) and by the International Organization for Standardization (ISO, IEC 60825-1:2014, European Union normative EN 60825-1:2014) (for determining the maximum permissible exposure MPE, the irradiance has been calculated considering a limiting circular aperture of 3.5 *mm* diameter) [50–52].

The DCSM is characterized by sixteen detection channels that are utilized to increase the signal-to-noise ratio in cases of low detected photon count-rates [53,54]. The intensity autocorrelation functions are calculated real time by a custom developed low-cost multi-channel (16 channels), multi-tau, fast (100 *Hz*) hardware auto-correlator made by four stackable and synchronized field programmable gated arrays (FPGA) of four channels each (HemoPhotonics, Castelldefels, Spain).

2.3. Ultrasound module (USM)

The LUCA ultrasound module is based on a commercial ultrasound device, EXAPad, produced by IMV Imaging, France [55]. EXAPad has a touchscreen interface, and allows several functionalities

such as B, B+B, B+M and M imaging, color Doppler, pulse wave and continuous wave Doppler modes.

The standard commercial EXAPad US module software has been modified by the manufacturer in order to deal with the communication with the main module and to manage the LUCA measurement protocol. In addition to the standard US functionalities, it includes a window tab dedicated to LUCA. Through this tab, the user connects the EXAPad module to the main module (via TCP/IP connection), in order to handle the data and image transfer to the optical main module, and to visualize and store the results of the optical measurements together with the US images acquired simultaneously. Moreover, it includes interfaces to start the optical measurement in "preview" mode, in order to check the optical data quality, and to run the optical measurement in "acquisition" mode. Lastly, the EXAPad module includes a section to review the images acquired and start the post-processing with the NIRFAST evaluation module (see below).

2.4. Multi-modal ultrasound-optical probe

The custom LUCA multi-modal optical-ultrasound probe has been developed by LUCA partner Vermon, France. It includes a standard US transducer commonly utilized for thyroid ultrasound (192 elements in the transducer, average sensitivity of 168 *mV*, a 70% relative bandwidth and a 10.6 *MHz* center frequency), and a chassis that allows the insertion of the optical fibers. The optical fiber tips are fixed to two replaceable fiber holders at the nose of the probe, one for the source fibers, and one for the detection fibers, placed next to the two long sides of the transducer (see Fig. 1(b)).

The design, together with the replaceable holders, allows flexibility for defining the geometry of the fiber tip positions, permitting the mounting of different holders with different geometries on the probe nose. The current geometry of the LUCA probe holders is reported in Fig. 1(b), together with a photo of the probe. Both DCS and TRS fiber configurations have two source-detector separations, the short distance, more sensitive to superficial layer properties, of 19 *mm* and the long, more sensitive to deeper tissue properties, of 25 *mm*. This configuration allows to simultaneously perform TRS and DCS measurements without crosstalk between the two technologies by reducing the effect of the DCS sources on TRS detectors and *vice versa* (see section 3.2). Furthermore, it is built around the standard US probe mechanics.

The TRS source fiber consists of a 100/140 *μm* core/cladding diameter graded index fiber, and the two detection patchcords consist in two fiber bundles of 168 graded index 100/140 *μm* core/cladding diameter fibers (long source-detector separation) and 213 graded index 62.5/125 *μm* core/cladding diameter fibers (short source-detector separation).

The DCS source at the probe nose consists of two 400 *μm* core fibers with ferrule termination placed at a reciprocal distance (center-to-center) of 4.4 *mm* in a symmetrical position respect to the detection fibers axis (see Fig. 1(b)). This particular configuration allows to roughly double the photon intensity detected by the DCS detectors, in compliance with the laser safety limits for tissue illumination, with respect to the standard configuration with a single DCS source fiber. The DCS detection fibers consist of a single mode fiber (for the wavelength of 785 *nm*) of 4.4/125 *μm* core/cladding diameter for the short source-detector separation, and in a bundle of fifteen single mode fibers (4.4/125 *μm* core/cladding diameter) for the long source-detector separation.

In addition, the LUCA probe includes a capacitive skin contact sensor, to detect bad coupling between the optical fiber tips at the probe nose and the skin, and an extra laser enable push button, which is used to enable the laser emission only when the probe is placed in a safe position on the tissue.

2.5. Post-processing, NIRFAST evaluation module (NEM)

The post-processing module consists of a custom assembled computer, with a graphics processing unit (GPU) utilizing CUDA (Compute Unified Device Architecture, Nvidia, U.S.A.) technology

supporting massive-parallelization in code execution [56,57]. Tissue parameter recovery is based on established NIRFAST software [48] package expanded with curve-fitting of TRS and DCS data using finite element method modelling. The NEM communicates through a network (TCP/IP) connection with the main module to receive the multi-modal data (the US images together with the optical raw data associated) and to return results (thyroid hemodynamic parameters and chromophore concentrations). The NIRFAST evaluation module is mounted in an independent 19" case, powered by a medical grade power supply. The post-processing system has been tested within the LUCA device environment on phantom and *in-vivo* data [58], and, as a sufficient number of subjects is recruited in the LUCA clinical campaign, the finite-elements solver of NIRFAST as well as its inversion algorithms will be utilized to model the curved and heterogeneous structures such as the trachea, carotid arteries as well as the thyroid tissue and the overlying muscles based on the ultrasound images. This will be the subject of a separate publication.

2.6. Main module (MM)

The main module is the principal control unit for the operation of the optical modules. It communicates with optical modules via USB connections, provides the real-time evaluation of optical data, and communicates with the ultrasound module via TCP/IP connection. We note that the user interacts with the LUCA device primarily through the USM. The operator can set optical evaluation parameters, supervise optical data quality and optical data acquisition in real time within the USM application, which requires such information from the MM. Additionally, the MM handles the requests for NEM post-processing via TCP/IP connection and stores optical and US data sets.

   The main functional units of the MM are: i) an industrial PC equipped with the required standard communication ports for USB and TCP/IP communication (ethernet port); ii) a custom electronic board for overall control including control of individual components of other modules. This board is equipped with a microcontroller and has been developed for the LUCA device for all lower level control lines (TTL) in order to enable/disable single module components, trigger options and safety features for the DCSM, TRSM as well as the LUCA probe. It includes several units of discrete safety electronics (for interlocks) and isolated readout/supply channels (for electrical safety) for probe electronics operation. The schematics of the Main Module connections with the other LUCA modules is reported in Fig. 1(c).

   In order to follow the modular concept of the LUCA device, the industrial PC and the microcontroller board are combined in an independent 19" case.

3. Device characterization

In this section we present the tests performed for the characterization of the LUCA device, mainly focusing on the optical modules. US module and the US probe, as well as any customization that was carried out, were tested by the manufacturers using standard procedures. Every module has been thoroughly tested individually and the whole LUCA device has been tested as a unique integrated system. Particular care has been dedicated to test the interference and cross-talk between all the different technologies working together in LUCA.

   Here, we report DCS and TRS phantom tests, and *in vivo* measurements such as repeatability in thyroid and arm cuff occlusion demonstration tests.

3.1. Analysis method for TRS and DCS acquisition

The reduced scattering (μ'_s) and absorption (μ_a) coefficients related to all the different wavelengths are retrieved from TRS acquisition by non-linear fitting of the solution of the diffusion equation for a semi-infinite homogeneous medium [59–61], convoluted with the instrument response

function (IRF) to the DTOF. The IRF is acquired separately for the long and short separation detection channels by placing in contact the tips of the source and detection fibers.

The effective Brownian diffusion coefficient D_B (for phantom measurements) and the blood flow index *BFi* (for *in vivo* measurements) have been retrieved by fitting of the solution of the electric field correlation diffusion equation for a semi-infinite homogeneous medium to the measured intensity auto-correlation functions [12]. The reduced scattering and absorption coefficients have first been obtained through TRS curve fitting, and then used as fixed parameters in the DCS curve fitting.

For retrieving the oxy and deoxy-hemoglobin changes (ΔHbO_2 and ΔHb) in the *in vivo* tests (see section 3.5), we have assumed linearity between absorption coefficients $\mu_a(\lambda)$ and the chromophore concentrations c_i, through the relation $\mu_a(\lambda) = \sum_i \epsilon_i(\lambda)c_i$, where ϵ_i is the *i*-th chromophore's extinction coefficient. The only parameters fitted were oxy and deoxy-hemoglobin concentrations, while water concentration has been kept fixed at 70% of the total chromophore concentration.

3.2. Integration of all the technologies

The optical and electronic interference between the two different diffuse optical technologies (TRS and DCS) and ultrasound has been evaluated during the design and the construction phases of the project. Additional precautions were taken whenever needed such as the insertion of notch and clean-up laser filters in TRSM and DCSM, and smart geometrical fiber disposition in the probe.

The effects that can reduce the quality of the acquisition are linked to the possible interference between US waves and optical acquisitions, between TRS sources and the DCS detectors, and between DCS sources and TRS detectors. In addition, we have tested the effect of the presence of the US coupling gel, in between the tissue and the probe, on the optical measurements quality. These last tests were the subject of a dedicated publication [62].

The cross-talk between US and optical acquisitions has been evaluated by performing measurements with the different modules alternatively turned on and off, and comparing these results to simultaneous acquisition. The results obtained demonstrates that TRS and DCS do not affect the quality of the US images, neither the presence of US waves affect the quality of TRS and DCS acquisitions (data not shown).

The cross-talk between TRS and DCS has been evaluated by measuring the background counts of DCS with TRS laser ON and OFF, in phantom and in thyroid (and, *vice versa*, by measuring the background counts of TRS with DCS laser ON and OFF). The phantom used consisted of a solid phantom based on epoxy resin with black toner as absorber and TiO_2 powder as scatterer [62,63], with reduced scattering coefficient of 10 cm^{-1} and absorption coefficient of 0.1 cm^{-1} at a wavelength of 660 *nm*. This situation is considered an extreme and unrealistic situation in the thyroid region, which is characterized by different optical properties (above all a much higher absorption, that reduces the effect of DCS laser on TRS detectors and *vice versa*) [10,47].

In Fig. 2(a) and (b), we have reported the effect of DCS laser on TRS acquisitions. While when measuring on the thyroid, the measured cross-talk between DCS and TRS is practically null (no background count-rate changes), we have registered an increase of approximately 100% of the TRS detector background when DCS source is turned on (background counts increases from ~ 50 *kcounts/s* to ~ 100 *kcounts/s*, after turning on DCS laser). As reported in Fig. 2(a) and (b), this increase does not affect the retrieval of the absorption and reduced scattering coefficients, since the TRS signal count-rate (roughly 1 *Mcounts/s*) assure in any case a good signal-to-noise-ratio. Lastly, with regard to DCS, the measured background changes (<0.3 *kcounts/s*) are negligible considering the common DCS count-rates in tissue and thyroid in particular (>10 *kcounts/s*) [10,12] and do not affect the acquisition. The minor differences (an

example is reported in Fig. 2(c)) are well below the variability associated to tissue physiological changes during the measurement.
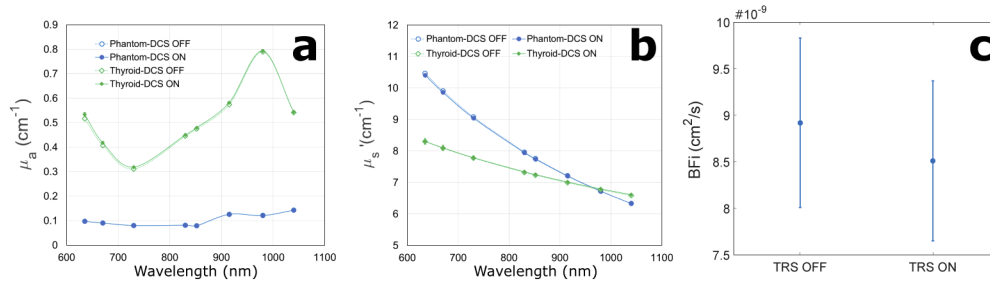

Fig. 2. Cross-talk between TRS and DCS. (a) Absorption coefficient measured by TRS in thyroid and phantom with DCS ON and OFF. (b) Reduced scattering coefficient measured by TRS in thyroid and phantom with DCS ON and OFF. (c) Blood flow index measured by DCS in thyroid with TRS ON and OFF

3.3. TRS phantom characterization

The time resolved spectroscopy module has been characterized and validated as an independent device through several phantom tests associated to the BIP, MEDPHOT and nEUROPt standardization protocols [63–66]. Preliminary results, related to the TRS as an independent stand-alone system, have already been published in a separate, dedicated publication [49]. Here we report a summary of the performance assessment standardization protocols (i.e. BIP, MEDPHOT and nEUROPt) implemented for the LUCA TRS integrated in the complete LUCA system. In order to not make this section heavier for the reader, the full set of results and detailed description of the tests performed have been reported in the Supplement 1.

BIP protocol characterizes the main features (source and detection components) of the TRS part of the LUCA device [64]. The optical power delivered to the sample (fully open attenuators) ranges from 0.62 *mW* (at 730 *nm*) up to 2.90 *mW* (at 830 *nm*). The responsivity of the detection chain is reported in the Supplement 1. Time to digital converter differential non linearity (*DNL* %) is around 15 % for both the detection channels. Finally, the afterpulsing ratio, *AR* %, was evaluated. We have estimated an afterpulsing ratio of few percent (from 0.6 % at 635 nm up to 8.5 % at 1040 nm), with a dependence on the wavelength probably due to the long decaying tail of the SiPM detectors. While this point will require further investigations, the small AR does not affect at all the reconstruction of the TRS data. Concluding, the TRS part of the device features an overall temporal resolution (FWHM of the instrument response function, IRF) ranging from 106 up to 193 *ps* depending on the wavelength, and it is stable over several hours (>6 hours) within an error 1 % of the average after thirty minutes from switching on of the device.

MEDPHOT protocol assesses the capability of the device to retrieve homogeneous optical properties of the tissue/sample under investigation. A 32 phantoms kit has been used to assess the linearity, accuracy and the reproducibility of the device [63]. From the tests performed we saw, as expected, a linear scaling of measured absorption and reduced scattering coefficients with respect to the nominal values of the phantoms used. The accuracy measured in retrieving the nominal absorption and reduced scattering coefficients is better than 20 % for the entire range of wavelengths.

The precision of the measured parameters μ'_s and μ_a, defined by the coefficient of variation $CV = 100 \cdot \sigma(x)/\langle x \rangle$ where x is the measured parameter, $\langle x \rangle$ its average value, and $\sigma(x)$ the standard deviation, is found to be better 1 % when the measurements are acquired at a count-rate higher than 200 *kcounts/s* at all the wavelengths. Moreover, we found *CV* for both absorption and

scattering, to be fairly in accordance with the ideal dependence $N^{-0.5}$, where N is the count-rate, which represents Poisson's noise contribution to the signal. Finally, the reproducibility of the retrieval of optical properties, obtained by repeating the measurement on the same phantom in different days, resulted better than 3 % for the absorption and 4 % for the scattering coefficient for both detection channels and at all the wavelengths. Overall, these values are within the requirements for successful *in vivo* use.

nEUROPt protocol evaluates the capability of a time resolved system to detect, localize, and quantify absorption changes within tissues. In this framework, phantoms with small black inclusions are used to mimic absorption changes [65,66]. As expected the maximum of contrast is obtained when the inclusion is below the probe and the value increases at later time-gates to finally drop due to the presence of the long time-constant tail of the SiPMs [67].

3.4. DCS phantom characterization

The DCS module has been thoroughly tested in the laboratory setting to assess its performance through liquid phantom experiments. A photo of the experimental setup is reported in Fig. 3(a). The stability of the system has been checked by measuring the Brownian diffusion coefficient D_B of a liquid phantom, over long time experiment (17 hours). The liquid phantom consists of a suspension of Lipofundin20% (B. Braun Melsungen AG, DE) in water, prepared following the recipe reported in Ref. [68] in order to have a reduced scattering coefficient of 5 cm^{-1} and water absorption. The measured D_B over time, related to one acquisition channel, at a photon count-rate of 200 $kcounts/s$, and average time 1 s, is reported in Fig. 3(b). The relative standard deviation over 17 hours measurement resulted <3%. In Fig. 3(c) we report the standard deviation of the reduced autocorrelation function ($g_2 - 1$), for all the acquisition channels over the whole measurement time. The results reported resulted in line with the state of the art diffuse correlation spectroscopy devices [35,69,70].

The capability of the LUCA DCS module to detect D_B changes has been proven by preparing a phantom with different viscosities obtained by adding glycerol in the suspension on Lipofundin20% in water [68], for different nominal values of reduced scattering coefficient (5, 10 and 15 cm^{-1}) and absorption coefficient (0.1, 0.2 and 0.3 cm^{-1}).

The particle Brownian diffusion coefficients related to the different phantoms have been measured and reported in Fig. 3(d) for the long source-detector separation channels, and (g) for the short one. Here, the values of the reduced scattering and absorption coefficients used in the DCS fitting procedure are measured simultaneously with LUCA TRS acquisition. This figure highlights the fact that, for increasing glycerol concentration, the measured particle Brownian diffusion coefficient decreases, as expected. Moreover, for highly absorbing and scattering phantoms, the Brownian diffusion coefficient measured results overestimated with respect to what is measured in phantoms with lower absorption and scattering. This behavior has been already reported in Ref. [69], and depends on the difficulty of determining the $\beta - factor$ in regime of low detected count-rates.

The capability of the LUCA DCS module to correctly measure changes in D_B results evident in Fig. 3(e) for the long source-detector separation channels - (h) for the short one - where we report the ratios of the measured D_B with the D_B of the 0% glycerol correspondent phantom, together with the expectation of the theory (i.e. $D_{B1}/D_{B2} = \eta_2/\eta_1$, where η is the viscosity of the solution [68,71]). We note that the accuracy of the recovered Brownian diffusion coefficient from these typical phantoms can be reliably assessed and is an ongoing topic of research [68,72–74].

Finally, in Fig. 3(f) and (i) the coefficient of variation CV of the retrieved D_B (obtained by averaging ten subsequent acquisitions on the same phantom) is reported for all the phantoms measured, for long and short source-detector separation respectively. The CV determines the precision of the D_B measurements, and it is mainly affected by the detected photon count-rate, that is lower for high scattering and absorption values.
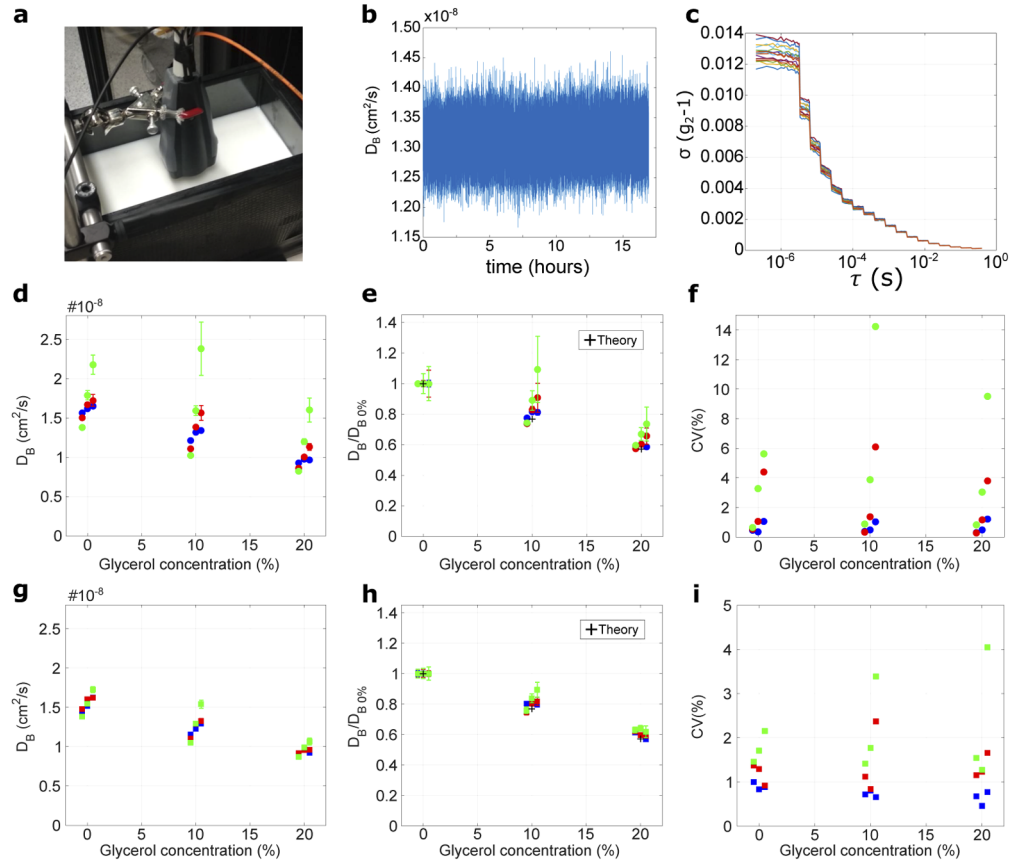
Fig. 3. DCS module phantom demonstration tests. (a) Photo of the experimental setup, with the LUCA probe fixed through a mechanical holder in vertical position over the liquid phantom box. (b) Stability of D_B over long time test (approx. 17 hours), data reported for one detection channel. (c) Standard deviation of the reduced autocorrelation function $(g_2 - 1)$, for all the 16 acquisition channels, over 17-hours stability test. (d) Measured D_B for phantom with different glycerol concentrations, long source-detector separation. (e) Ratio of the measured D_B for phantom with different glycerol concentration (i. e. different viscosity) and comparison with theory, long source-detector separation. (f) Precision (*CV*) of the measured D_B for phantom with different glycerol concentration (i. e. different viscosity), long source-detector separation. Different colors represent solutions with different absorption coefficient (blue $\mu_a = 0.1\ cm^{-1}$, red $\mu_a = 0.2\ cm^{-1}$, green $\mu_a = 0.3\ cm^{-1}$), while the displacement with respect to the vertical axis represents different reduced scattering coefficients (left displacement: $\mu'_s = 5\ cm^{-1}$, center: $\mu'_s = 10\ cm^{-1}$, right displacement: $\mu'_s = 15\ cm^{-1}$). (g), (h), and (i) same as (d), (e) and (f) but for short source-detector separation channel.

3.5. In vivo characterization

3.5.1. Variability on thyroid

To assess the precision of the LUCA device in measuring the optical and hemodynamic properties of the thyroid tissue, repeatability tests have been performed. The same thyroid lobe of the same healthy volunteer has been measured in four different days in two consecutive weeks. Each day, we have performed five independent measurements of the same lobe, by removing and replacing the LUCA probe on the same position of the volunteer neck. By looking at the real time US images of neck, the operator was able to find the same position after every probe replacement. This operation requires approximately one minute of time. The LUCA probe has been fixed to volunteer neck in a stable position through a mechanical arm, that reduces the artefacts due to probe movements along the duration of each single acquisition (approximately 100 s). In addition, artefacts in the signal clearly due to subject movements, have been detected and removed when processing the data. In Fig. 4(a) we report images of the experimental configuration adopted for the *in vivo* repeatability tests. In Fig. 4 (b) we show an US image of the thyroid of the healthy voluntary subject, acquired simultaneously to the optical acquisition.
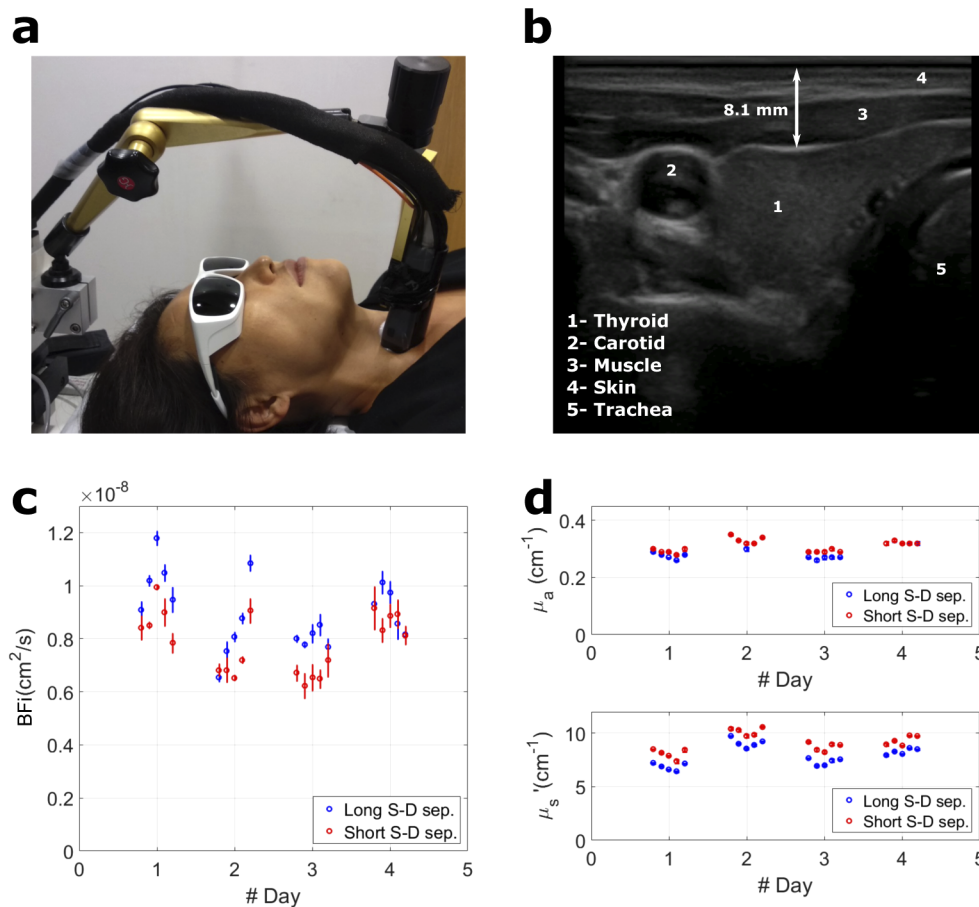
Fig. 4. *In vivo* tests. (a) Set up for thyroid repeatability measurements. (b) US image acquired simultaneously with optical data: 1- thyroid right lobe; 2- carotid; 3- sternocleidomastoid muscle; 4- skin; 5- trachea. (c) DCS repeatability results in the right thyroid lobe (5 repetitions per day, 4 days of measurements). (d) TRS repeatability results in the right thyroid lobe, absorption coefficient (top) and reduced scattering coefficient (bottom).

The main results of the thyroid repeatability tests are summarized in Table 1 for the DCS and Tables 2, 3 and 4 for the TRS, and reported graphically in Fig. 4(c) (DCS) and (d) (TRS). Overall, these preliminary results in thyroid are in line with what was reported in Ref. [10]. A deeper quantitative comparison with previous literature *in vivo* results falls beyond the scope of this work, and will be available as the LUCA clinical research campaign, currently ongoing, reaches a sufficient number of recruited subjects. Furthermore, we note that at this stage, a comparison of our preliminary results with clinical gold standards is challenging. In fact, microvascular blood flow in the thyroid and nodules has not been thoroughly evaluated apart from only a pilot study utilizing arterial spin labelled magnetic resonance imaging, reporting significant changes in nodules [75,76].

Table 1. Variability of *BFi* measured in thyroid.

S-D separation (mm)	CV single acquisition (%)	CV single day (%)	CV between days (%)
25	3.0	10.6	10.8
19	3.5	8.3	13.3

Table 2. Variability of TRS measured parameters at all wavelengths in a single measurement in thyroid.

Parameter	S-D sep. (mm)	CV_{635} (%)	CV_{670} (%)	CV_{730} (%)	CV_{830} (%)	CV_{852} (%)	CV_{915} (%)	CV_{980} (%)	CV_{1040} (%)
μ_a	25	1.28	1.20	1.03	1.26	1.06	1.08	0.75	1.08
μ_a	19	1.45	1.25	1.07	1.05	0.95	0.89	0.53	0.95
μ_s'	25	1.21	0.75	1.21	0.88	0.95	0.91	0.75	0.98
μ_s'	19	0.87	0.68	1.04	0.81	0.83	0.79	0.67	0.91

Table 3. Variability of TRS measured parameters at all wavelengths in a single day in thyroid.

Parameter	S-D sep. (mm)	CV_{635} (%)	CV_{670} (%)	CV_{730} (%)	CV_{830} (%)	CV_{852} (%)	CV_{915} (%)	CV_{980} (%)	CV_{1040} (%)
μ_a	25	3.44	3.70	3.33	2.76	2.51	2.24	1.54	2.77
μ_a	19	2.48	2.05	2.36	1.82	1.93	1.71	1.70	2.07
μ_s'	25	4.19	4.04	4.01	3.71	3.83	3.66	2.92	3.78
μ_s'	19	3.31	3.68	4.28	3.96	3.91	3.98	2.95	4.25

Table 4. Variability of TRS measured parameters at all wavelengths between days in thyroid.

Parameter	S-D sep. (mm)	CV_{635} (%)	CV_{670} (%)	CV_{730} (%)	CV_{830} (%)	CV_{852} (%)	CV_{915} (%)	CV_{980} (%)	CV_{1040} (%)
μ_a	25	9.52	9.43	9.77	7.99	7.78	7.97	4.60	8.01
μ_a	19	8.10	5.32	6.24	7.82	5.15	4.82	3.50	7.14
μ_s'	25	14.33	11.84	12.35	12.08	12.00	13.43	12.62	13.58
μ_s'	19	7.86	9.59	10.62	12.41	10.22	10.55	10.85	12.15

In the tables we have reported the coefficient of variation *CV*. The DCS repeatability tests highlight a variability of the single DCS acquisition of 3% approximately, an inter-repetition variability of 10%, approximately the same as the variability between the *BFi* values measured in

different days. The variability of less than 3% for a single DCS acquisition is considerably good in light of the low number of photons detectable from the thyroid tissue, characterized by high absorption [10,47]. This high quality result is made possible by the configuration of the probe - considering two identical source outputs placed in a symmetrical position with respect to detector fibers ($x - y$ in Fig. 1(b)), helping in increasing the photon count-rate - and by the possibility of averaging signals simultaneously acquired from 16 independent detection channels [53,54].

The TRS repeatability tests assess that the absorption coefficient has a single measurement variability <2%, a variability between different measurements (probe replacement) <4%, and a variability between different days <10%. The reduced scattering coefficient shows a single measurement variability <2%, a variability between different measurements (probe replacement) <5%, and a variability between different days <15%. In Fig. 4(d) the results of the repeatability tests for a single exemplary wavelength (730 *nm*), for absorption (top panel) and reduced scattering coefficient (bottom panel) are shown.

3.5.2. Arm cuff demonstration

The capability of LUCA device in detecting changes in hemodynamics has been proved by measuring the arm muscle during an arterial cuff occlusion challenge. Since the LUCA device has been designed to perform measurements in stationary physiological condition, and does not have a high acquisition rate, we have decided to acquire with TRS just two wavelengths, 670 and 830 *nm*, of the eight available, in order to be able to recover the oxy- and deoxy-hemoglobin concentration changes while maintaining an acceptable temporal resolution (roughly an acquisition every 7 seconds). The LUCA probe has been placed in contact with the arm muscle, and a baseline signal has been acquired for roughly three minutes. Then we have applied a cuff pressure of 180 *mmHg* for three minutes, and, lastly, we measured the recovery signal, releasing the cuff pressure, for roughly 5 minutes. In Fig. 5 we report the results of the arm cuff demonstration test. In panel (a) the relative blood flow index is reported, while in the (b) panel the oxy and deoxy hemoglobin changes are reported, for both the long and short source-detector distances. The high quality results reported demonstrate that the LUCA device is able to follow temporal hemodynamic changes with a high dynamic range, well in agreement with previous literature [35,61,70].
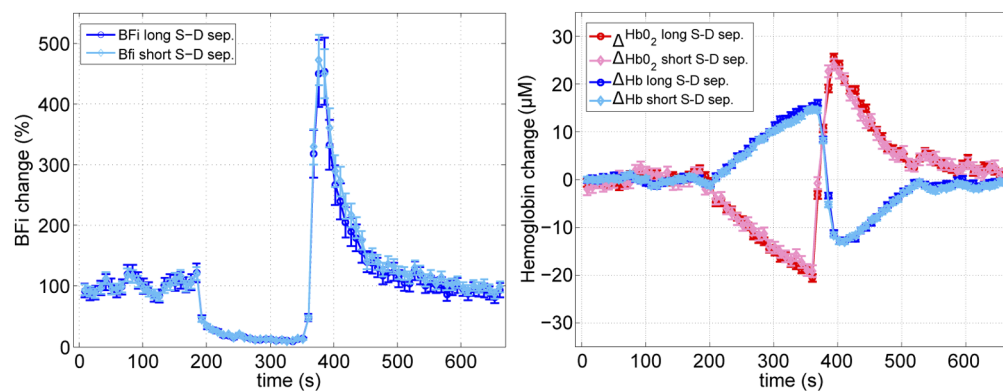

Fig. 5. Arm cuff occlusion demonstration test. Blood flow index (*BFi*) changes (left block) and oxy- and deoxy-hemoglobin change (right block)

4.   Discussion and conclusion

In conclusion, we have presented and characterized, through phantom and *in vivo* performance tests, the LUCA device.

The LUCA device is a unique optical-ultrasound clinical platform, developed in collaboration between academia, industry and clinicians, that combines hemodynamic and tissue constituent information, provided by TRS and DCS, in a way that could be incorporated within the standard, clinical thyroid cancer screening workflow, that is ultrasound imaging.

Overall, the LUCA device validation tests have demonstrated the capability of the system of performing high quality clinical measurements.

The optical subsystems are composed mainly by custom developed components that contribute significantly to reduce the costs with respect to standard commercially available ones, while maintaining very high performances. The DCS module, despite the reduction of costs due to completely new hardware components, is capable of performing high quality measurements even with low photon count-rates, allowing the simultaneous acquisition of 16 independent detection channels. The TRS module consists of custom made laser heads and electronics, detectors and acquisition electronics, reducing the costs by a factor of 4-8 compared to equivalent commercially available components, while maintaining excellent performances.

The LUCA device's clinical ultrasound imaging modality, in addition to providing anatomical information for the standard clinical thyroid cancer screening process, plays a role of guiding the probe on the right region of interest, reducing the in-determination due to probe misplacements for the optical measurements. In future, the anatomical US information can be used to further enhance the TRS/DCS analysis. Indeed, the LUCA device allows the radiologist to select the measurements of interest, draw different structures (e.g., trachea, thyroid, nodule, carotid) on the ultrasound images and then receive a report of analyzed data which is mimicked by this post-processing method. This is expected to improve the precision and accuracy of the optical data analysis and provide clinically useful measurement to enhance disease identification and prognosis. The use and effectiveness of these advanced methods requires detailed validation, and the correspondent study is still underway.

Concluding, the LUCA device was developed and tested for the clinical application in the field of endocrinology, where there is the necessity of improving the current standard of thyroid cancer diagnosis. Nevertheless, given the recent advances of diffuse optical techniques, the LUCA device can find potential application in several different fields, as for example breast, head and neck, abdominal cancers diagnosis and therapy monitoring, where the multi-modal approach involving simultaneous ultrasound imaging can produce a fundamental improvement in the quality of the examination.

Appendix A. The LUCA consortium

Laser and Ultrasound Co-analyzer for Thyroid Nodules (LUCA) project is supported by European Union's Horizon 2020 research and innovation programme and aims to develop an innovative technology for thyroid cancer screening that will provide doctors with enhanced information required to provide better and more specific results in thyroid nodule screening and enable better diagnosis.

The LUCA consortium is a multidisciplinary team including clinical endocrinologists, radiologists, physicists, engineers and industry players. The LUCA consortium is coordinated by the Institute of Photonic Sciences (ICFO, Barcelona, Spain). The academic/clinical partners (in addition to ICFO) are: Politecnico di Milano (POLIMI, Milan, Italy), University of Birmingham (Birmingham, U.K.) and Institut d'Investigacions Biomèdiques August Pi i Sunyer - IDIBAPS/Hospital Clínic (Barcelona, Spain). The industrial partners are: Hemophotonics S.L. (Castelldefels, Spain), Vermon SA (Tours, France) and IMV imaging (Angoulême, France). In

addition, the LUCA consortium includes the European Institute for Biomedical Research (EIBIR, Wien, Austria), for the project management and dissemination. For further information, please see the project web-site at http://www.luca-project.eu.

Disclosures. The role in the project of all the companies and their employees involved has been defined by the project objectives, tasks, and work packages and has been reviewed by the European Commission. MB, DC, ADM, AT are co-founders of pioNIRS s.r.l., spin off company from Politecnico di Milano (Italy). Potential financial conflicts of interest and objectivity of research have been monitored by ICFO's Knowledge & Technology Transfer Department.

Data availability. Data underlying the results presented in this paper are not publicly available at this time but may be obtained from the authors upon reasonable request.

Supplemental document. See Supplement 1 for supporting content.

References

1. Q. Zhu, T. Durduran, V. Ntziachristos, M. Holboke, and A. Yodh, "Imager that combines near-infrared diffusive light and ultrasound," Opt. Lett. **24**(15), 1050–1052 (1999).
2. Q. Zhu, D. Sullivan, B. Chance, and T. Dambro, "Combined ultrasound and near infrared diffused light imaging in a test object," IEEE Trans. Ultrason., Ferroelect., Freq. Contr. **46**(3), 665–678 (1999).
3. M. J. Holboke, B. J. Tromberg, X. Li, N. Shah, J. Fishkin, D. Kidney, J. Butler, B. Chance, and A. G. Yodh, "Three-dimensional diffuse optical mammography with ultrasound localization in a human subject," J. Biomed. Opt. **5**(2), 237–247 (2000).
4. N. G. Chen, P. Guo, S. Yan, D. Piao, and Q. Zhu, "Simultaneous near-infrared diffusive light and ultrasound imaging," Appl. Opt. **40**(34), 6367–6380 (2001).
5. Q. Zhu, "Combined ultrasound and near infrared diffused light imaging system," (2001). US Patent 6, 264, 610.
6. Q. Zhu, M. Huang, N. Chen, K. Zarfos, B. Jagjivan, M. Kane, P. Hedge, and H. S. Kurtzman, "Ultrasound-guided optical tomographic imaging of malignant and benign breast lesions: initial clinical results of 19 cases," Neoplasia **5**(5), 379–388 (2003).
7. Q. Zhu, S. H. Kurtzman, P. Hegde, S. Tannenbaum, M. Kane, M. Huang, N. G. Chen, B. Jagjivan, and K. Zarfos, "Utilizing optical tomography with ultrasound localization to image heterogeneous hemoglobin distribution in large breast cancers," Neoplasia **7**(3), 263–270 (2005).
8. Q. Zhu, E. B. Cronin, A. A. Currier, H. S. Vine, M. Huang, N. Chen, and C. Xu, "Benign versus malignant breast masses: optical differentiation with us-guided optical imaging reconstruction," Radiology **237**(1), 57–66 (2005).
9. Q. Zhu, P. A. DeFusco, A. Ricci Jr, E. B. Cronin, P. U. Hegde, M. Kane, B. Tavakoli, Y. Xu, J. Hart, and S. H. Tannenbaum, "Breast cancer: assessing response to neoadjuvant chemotherapy by using us-guided near-infrared tomography," Radiology **266**(2), 433–442 (2013).
10. C. Lindner, M. Mora, P. Farzam, M. Squarcia, J. Johansson, U. M. Weigel, I. Halperin, F. A. Hanzu, and T. Durduran, "Diffuse optical characterization of the healthy human thyroid tissue and two pathological case studies," PLoS One **11**(1), e0147851 (2016).
11. L. Wang, N. Schwartz, J. M. Cochran, T. Ko, W. Baker, L. He, K. Abramson, and A. Yodh, "Noninvasive measurement of placental hemodynamics with ultrasound-guided fd-diffuse optical spectroscopy," in *Biophotonics Congress: Biomedical Optics 2020 (Translational, Microscopy, OCT, OTS, BRAIN)* (Optical Society of America, 2020), p. SW4D.5.
12. T. Durduran, R. Choe, W. B. Baker, and A. G. Yodh, "Diffuse optics for tissue monitoring and tomography," Rep. Prog. Phys. **73**(7), 076701 (2010).
13. A. Yodh and B. Chance, "Spectroscopy and imaging with diffusing light," Phys. Today **48**(3), 34–40 (1995).
14. B. J. Tromberg, N. Shah, R. Lanning, A. Cerussi, J. Espinoza, T. Pham, L. Svaasand, and J. Butler, "Non-invasive in vivo characterization of breast tumors using photon migration spectroscopy," Neoplasia **2**(1-2), 26–40 (2000).
15. V. Ntziachristos, A. Yodh, M. Schnall, and B. Chance, "Concurrent mri and diffuse optical tomography of breast after indocyanine green enhancement," Proc. Natl. Acad. Sci. **97**(6), 2767–2772 (2000).
16. D. A. Boas, A. M. Dale, and M. A. Franceschini, "Diffuse optical imaging of brain activation: approaches to optimizing image sensitivity, resolution, and accuracy," NeuroImage **23**, S275–S288 (2004).
17. M. A. Franceschini, S. Thaker, G. Themelis, K. K. Krishnamoorthy, H. Bortfeld, S. G. Diamond, D. A. Boas, K. Arvin, and P. E. Grant, "Assessment of infant brain development with frequency-domain near-infrared spectroscopy," Pediatr. Res. **61**(5, Part 1), 546–551 (2007).

18. G. Yu, T. Durduran, G. Lech, C. Zhou, B. Chance, E. R. Mohler, and A. G. Yodh, "Time-dependent blood flow and oxygenation in human skeletal muscles measured with noninvasive near-infrared diffuse optical spectroscopies," J. Biomed. Opt. **10**(2), 024027 (2005).

19. M. Ferrari and V. Quaresima, "A brief review on the history of human functional near-infrared spectroscopy (fnirs) development and fields of application," NeuroImage **63**(2), 921–935 (2012).

20. M. Wolf, M. Ferrari, and V. Quaresima, "Progress of near-infrared spectroscopy and topography for brain and muscle clinical applications," J. Biomed. Opt. **12**(6), 062104 (2007).

21. G. Bale, C. E. Elwell, and I. Tachtsidis, "From jöbsis to the present day: a review of clinical near-infrared spectroscopy measurements of cerebral cytochrome-c-oxidase," J. Biomed. Opt. **21**(9), 091307 (2016).

22. M. S. Patterson, B. Chance, and B. C. Wilson, "Time resolved reflectance and transmittance for the non- invasive measurement of tissue optical properties," Appl. Opt. **28**(12), 2331–2336 (1989).

23. A. Pifferi, D. Contini, A. Dalla Mora, A. Farina, L. Spinelli, and A. Torricelli, "New frontiers in time-domain diffuse optics, a review," J. Biomed. Opt. **21**(9), 091310 (2016).

24. A. Dalla Mora, D. Contini, S. Arridge, F. Martelli, A. Tosi, G. Boso, A. Farina, T. Durduran, E. Martinenghi, A. Torricelli, and A. Pifferi, "Towards next-generation time-domain diffuse optics for extreme depth penetration and sensitivity," Biomed. Opt. Express **6**(5), 1749 (2015).

25. S. Konugolu Venkata Sekar, I. Bargigia, A. Dalla Mora, P. Taroni, A. Ruggeri, A. Tosi, A. Pifferi, and A. Farina, "Diffuse optical characterization of collagen absorption from 500 to 1700 nm," J. Biomed. Opt. **22**(1), 015006 (2017).

26. A. Pifferi, A. Farina, A. Torricelli, G. Quarto, R. Cubeddu, and P. Taroni, "Time-domain broadband near infrared spectroscopy of the female breast: a focused review from basic principles to future perspectives," J. Near Infrared Spectrosc. **20**(1), 223–235 (2012).

27. P. Taroni, A. Pifferi, A. Torricelli, D. Comelli, and R. Cubeddu, "In vivo absorption and scattering spectroscopy of biological tissues," Photochem. Photobiol. Sci. **2**(2), 124–129 (2003).

28. A. M. Nilsson, C. Sturesson, D. L. Liu, and S. Andersson-Engels, "Changes in spectral shape of tissue optical properties in conjunction with laser-induced thermotherapy," Appl. Opt. **37**(7), 1256–1267 (1998).

29. D. A. Boas, L. E. Campbell, and A. G. Yodh, "Scattering and imaging with diffusing temporal field correlations," Phys. Rev. Lett. **75**(9), 1855–1858 (1995).

30. D. A. Boas and A. G. Yodh, "Spatially varying dynamical properties of turbid media probed with diffusing temporal light correlation," J. Opt. Soc. Am. A **14**(1), 192 (1997).

31. E. M. Buckley, A. B. Parthasarathy, P. E. Grant, A. G. Yodh, and M. A. Franceschini, "Diffuse correlation spectroscopy for measurement of cerebral blood flow: future prospects," Neurophotonics **1**(1), 011009 (2014).

32. L. He, W. B. Baker, D. Milej, V. C. Kavuri, R. C. Mesquita, D. R. Busch, K. Abramson, J. Y. Jiang, M. Diop, K. S. Lawrence, O. Amendolia, F. Quattrone, R. Balu, W. A. Kofke, and A. G. Yodh, "Noninvasive continuous optical monitoring of absolute cerebral blood flow in critically ill adults," Neurophotonics **5**(4), 045006 (2018).

33. D. Milej, M. Shahid, A. Abdalmalak, A. Rajaram, M. Diop, and K. S. Lawrence, "Characterizing dynamic cerebral vascular reactivity using a hybrid system combining time-resolved near-infrared and diffuse correlation spectroscopy," Biomed. Opt. Express **11**(8), 4571–4585 (2020).

34. N. Roche-Labarbe, S. A. Carp, A. Surova, M. Patel, D. A. Boas, P. E. Grant, and M. A. Franceschini, "Noninvasive optical measures of cbv, sto2, cbf index, and rcmro2 in human premature neonates' brains in the first six weeks of life," Hum. Brain Mapp. **31**(3), 341–352 (2010).

35. M. Giovannella, "BabyLux device: a diffuse optical system integrating diffuse correlation spectroscopy and time-resolved near-infrared spectroscopy for the neuromonitoring of the premature newborn brain," Neurophotonics **6**(02), 1 (2019).

36. R. Choe and T. Durduran, "Diffuse optical monitoring of the neoadjuvant breast cancer therapy," IEEE J. Sel. Top. Quantum Electron. **18**(4), 1367–1386 (2012).

37. G. Yu, "Near-infrared diffuse correlation spectroscopy in cancer diagnosis and therapy monitoring," J. Biomed. Opt. **17**(1), 010901 (2012).

38. V. Quaresima, P. Farzam, P. Anderson, P. Y. Farzam, D. Wiese, S. A. Carp, M. Ferrari, and M. A. Franceschini, "Diffuse correlation spectroscopy and frequency-domain near-infrared spectroscopy for measuring microvascular blood flow in dynamically exercising human muscles," J. Appl. Physiol. **127**(5), 1328–1337 (2019).

39. http://www.luca-project.eu.

40. B. R. Haugen, E. K. Alexander, K. C. Bible, G. M. Doherty, S. J. Mandel, Y. E. Nikiforov, F. Pacini, G. W. Randolph, A. M. Sawka, M. Schlumberger, K. G. Schuff, S. I. Sherman, J. A. Sosa, D. L. Steward, R. M. Tuttle, and L. Wartofsky, "2015 American thyroid association management guidelines for adult patients with thyroid nodules and differentiated thyroid cancer: the Aamerican thyroid association guidelines task force on thyroid nodules and differentiated thyroid cancer," Thyroid **26**(1), 1–133 (2016).

41. F. Bray, J. Ferlay, I. Soerjomataram, R. L. Siegel, L. A. Torre, and A. Jemal, "Global cancer statistics 2018: GLOBOCAN estimates of incidence and mortality worldwide for 36 cancers in 185 countries," CA: A Cancer Journal for Clinicians **68**(6), 394–424 (2018).

42. T. Rago, G. Di Coscio, F. Basolo, M. Scutari, R. Elisei, P. Berti, P. Miccoli, R. Romani, P. Faviana, A. Pinchera, and P. Vitti, "Combined clinical, thyroid ultrasound and cytological features help to predict thyroid malignancy in follicular and Hrthle cell thyroid lesions: results from a series of 505 consecutive patients," Clin. Endocrinol. p. 061109020454002 (2006).

43. I. S. Nam-Goong, H. Y. Kim, G. Gong, H. K. Lee, S. J. Hong, W. B. Kim, and Y. K. Shong, "Ultrasonography-guided fine-needle aspiration of thyroid incidentaloma: correlation with pathological findings," Clin. Endocrinol. **60**(1), 21–28 (2004).

44. J. A. Sipos, "Advances in ultrasound for the diagnosis and management of thyroid cancer," Thyroid **19**(12), 1363–1372 (2009).

45. M. Appetecchia and F. Solivetti, "The association of colour flow doppler sonography and conventional ultrasonography improves the diagnosis of thyroid carcinoma," Horm. Res. Paediatr. **66**(5), 249–256 (2006).

46. B. McIver, "Evaluation of the thyroid nodule," Oral Oncol. **49**(7), 645–653 (2013).

47. S. Konugolu Venkata Sekar, A. Farina, A. Dalla Mora, C. Lindner, M. Pagliazzi, M. Mora, G. Aranda, H. Dehghani, T. Durduran, P. Taroni, and A. Pifferi, "Broadband (550-1350 nm) diffuse optical characterization of thyroid chromophores," Sci. Rep. **8**(1), 10015 (2018).

48. H. Dehghani, M. E. Eames, P. K. Yalavarthy, S. C. Davis, S. Srinivasan, C. M. Carpenter, B. W. Pogue, and K. D. Paulsen, "Near infrared optical tomography using nirfast: Algorithm for numerical model and image reconstruction," Commun. Numer. Meth. Engng. **25**(6), 711–732 (2009).

49. M. Renna, M. Buttafava, A. Behera, M. Zanoletti, L. Di Sieno, A. Dalla Mora, D. Contini, and A. Tosi, "Eight-wavelength, dual detection channel instrument for near-infrared time-resolved diffuse optical spectroscopy," IEEE J. Sel. Top. Quantum Electron. **25**(1), 1–11 (2019).

50. A. N. S. Institute, *American national standard for safe use of lasers: ANSI Z136.1-2014* (Laser Institute of America, 2014).

51. Standard IEC 60825-1:2014, International Organization for Standardization.

52. D. R. Busch, J. Davis, A. Kogler, R. M. Galler, A. B. Parthasarathy, A. G. Yodh, and T. F. Floyd, "Laser safety in fiber-optic monitoring of spinal cord hemodynamics: a preclinical evaluation," J. Biomed. Opt. **23**(06), 1–9 (2018).

53. G. Dietsche, M. Ninck, C. Ortolf, J. Li, F. Jaillon, and T. Gisler, "Fiber-based multispeckle detection for time-resolved diffusing-wave spectroscopy: characterization and application to blood flow detection in deep tissue," Appl. Opt. **46**(35), 8506 (2007).

54. L. Cortese, G. Lo Presti, M. Pagliazzi, D. Contini, A. Dalla Mora, H. Dehghani, F. Ferri, F. J. B. M. Giovannella, F. Martelli, U. M. Weigel, S. Wojtkiewicz, M. Zanoletti, and T. Durduran, "Recipes for diffuse correlation spectroscopy instrument design using commonly utilized hardware based on targets for signal-to-noise ratio and precision," Biomed. Opt. Express **12**(6), 3265–3281 (2021).

55. This device is currently commercialized for medical applications by Quantel Medical (Cournon d'Auvergne, France) under the EvoTouch+ product brand.

56. M. Doulgerakis-Kontoudis, A. T. Eggebrecht, S. Wojtkiewicz, J. P. Culver, and H. Dehghani, "Toward real-time diffuse optical tomography: accelerating light propagation modeling employing parallel computing on gpu and cpu," J. Biomed. Opt. **22**(12), 125001 (2017).

57. S. Wojtkiewicz, T. Durduran, and H. Dehghani, "Time-resolved near infrared light propagation using frequency domain superposition," Biomed. Opt. Express **9**(1), 41–54 (2018).

58. S. Wojtkiewicz, U. M. Weigel, T. Durduran, and H. Dehghani, "Cloud-based nirfast server for tissue parameters recovery: laser and ultrasound co-analyser of thyroid nodules," in *Diffuse Optical Spectroscopy and Imaging VII*, vol. 11074 (International Society for Optics and Photonics, 2019), p. 110740L.

59. R. C. Haskell, L. O. Svaasand, T.-T. Tsay, T.-C. Feng, B. J. Tromberg, and M. S. McAdams, "Boundary conditions for the diffusion equation in radiative transfer," J. Opt. Soc. Am. A **11**(10), 2727 (1994).

60. D. Contini, F. Martelli, and G. Zaccanti, "Photon migration through a turbid slab described by a model based on diffusion approximation. i. theory," Appl. Opt. **36**(19), 4587–4599 (1997).

61. R. Re, I. Pirovano, D. Contini, L. Spinelli, and A. Torricelli, "Time domain near infrared spectroscopy device for monitoring muscle oxidative metabolism: Custom probe and in vivo applications," Sensors **18**(1), 264 (2018).

62. L. Di Sieno, D. Contini, G. Lo Presti, L. Cortese, T. Mateo, B. Rosinski, E. Venturini, P. Panizza, M. Mora, G. Aranda, M. Squarcia, A. Farina, T. Durduran, P. Taroni, A. Pifferi, and A. Dalla Mora, "Systematic study of the effect of ultrasound gel on the performances of time-domain diffuse optics and diffuse correlation spectroscopy," Biomed. Opt. Express **10**(8), 3899 (2019).

63. A. Pifferi, A. Torricelli, A. Bassi, P. Taroni, R. Cubeddu, H. Wabnitz, D. Grosenick, M. Möller, R. Macdonald, J. Swartling, T. Svensson, S. Andersson-Engels, R. L. P. van Veen, H. J. C. M. Sterenborg, J.-M. Tualle, H. L. Nghiem, S. Avrillier, M. Whelan, and H. Stamm, "Performance assessment of photon migration instruments: the medphot protocol," Appl. Opt. **44**(11), 2104–2114 (2005).

64. H. Wabnitz, D. R. Taubert, M. Mazurenka, O. Steinkellner, A. Jelzow, R. Macdonald, D. Milej, P. Sawosz, M. Kacprzak, A. Liebert, R. Cooper, J. Hebden, A. Pifferi, A. Farina, I. Bargigia, D. Contini, M. Caffini, L. Zucchelli, L. Spinelli, R. Cubeddu, and A. Torricelli, "Performance assessment of time-domain optical brain imagers, part 1: basic instrumental performance protocol," J. Biomed. Opt. **19**(8), 086010 (2014).

65. H. Wabnitz, A. Jelzow, M. Mazurenka, O. Steinkellner, R. Macdonald, D. Milej, N. Żołek, M. Kacprzak, P. Sawosz, R. Maniewski, A. Liebert, S. Magazov, J. C. Hebden, F. Martelli, P. D. Ninni, G. Zaccanti, A. Torricelli, D. Contini, R. Re, L. M. Zucchelli, L. Spinelli, R. Cubeddu, and A. Pifferi, "Performance assessment of time-domain optical brain imagers, part 2: neuropt protocol," J. Biomed. Opt. **19**(8), 086012 (2014).

66. A. Pifferi, A. Torricelli, R. Cubeddu, G. Quarto, R. Re, S. K. Sekar, L. Spinelli, A. Farina, F. Martelli, and H. Wabnitz, "Mechanically switchable solid inhomogeneous phantom for performance tests in diffuse imaging and spectroscopy," J. Biomed. Opt. **20**(12), 121304 (2015).

67. E. Martinenghi, A. Dalla Mora, D. Contini, A. Farina, F. Villa, A. Torricelli, and A. Pifferi, "Spectrally resolved single-photon timing of silicon photomultipliers for time-domain diffuse spectroscopy," IEEE Photonics J. **7**(4), 1–12 (2015).

68. L. Cortese, G. L. Presti, M. Pagliazzi, D. Contini, A. Dalla Mora, A. Pifferi, S. K. V. Sekar, L. Spinelli, P. Taroni, M. Zanoletti, U. M. Weigel, S. de Fraguier, A. Nguyen-Dihn, B. Rosinski, and T. Durduran, "Liquid phantoms for near-infrared and diffuse correlation spectroscopies with tunable optical and dynamic properties," Biomed. Opt. Express **9**(5), 2068 (2018).

69. M. Giovannella, L. Spinelli, M. Pagliazzi, D. Contini, G. Greisen, U. M. Weigel, A. Torricelli, and T. Durduran, "Accuracy and precision of tissue optical properties and hemodynamic parameters estimated by the BabyLux device: a hybrid time-resolved near-infrared and diffuse correlation spectroscopy neuro-monitor," Biomed. Opt. Express **10**(5), 2556 (2019).

70. S. A. Carp, P. Farzam, N. Redes, D. M. Hueber, and M. A. Franceschini, "Combined multi-distance frequency domain and diffuse correlation spectroscopy system with simultaneous data acquisition and real-time analysis," Biomed. Opt. Express **8**(9), 3993 (2017).

71. "Physical Properties of Glycerine and Its Solutions," Glycerine Producers Association (1963).

72. C. Amendola, M. Lacerenza, M. Buttafava, A. Tosi, L. Spinelli, D. Contini, and A. Torricelli, "A compact multi-distance dcs and time domain nirs hybrid system for hemodynamic and metabolic measurements," Sensors **21**(3), 870 (2021).

73. S. A. Carp, D. Tamborini, D. Mazumder, K.-C. Wu, M. B. Robinson, K. A. Stephens, O. Shatrovoy, N. Lue, N. Ozana, M. H. Blackwell, and M. A. Franceschini, "Diffuse correlation spectroscopy measurements of blood flow using 1064 nm light," J. Biomed. Opt. **25**(09), 1–15 (2020).

74. S. Samaei, P. Sawosz, M. Kacprzak, Ź Pastuszak, D. Borycki, and A. Liebert, "Time-domain diffuse correlation spectroscopy (td-dcs) for noninvasive, depth-dependent blood flow quantification in human tissue in vivo," Sci. Rep. **11**(1), 1817 (2021).

75. C. Schraml, A. Boss, P. Martirosian, N. F. Schwenzer, C. D. Claussen, and F. Schick, "Fair true-fisp perfusion imaging of the thyroid gland," J. Magn. Reson. Imaging **26**(1), 66–71 (2007).

76. C. Schraml, K. Müssig, P. Martirosian, N. F. Schwenzer, C. D. Claussen, H.-U. Häring, B. M. Balletshofer, and F. Schick, "Autoimmune thyroid disease: arterial spin-labeling perfusion mr imaging," Radiology **253**(2), 435–442 (2009).